Metasurface-based bijective illumination collection imaging provides high-resolution tomography in three dimensions

Masoud Pahlevaninezhad[1,4,5], **Yao-Wei Huang**[2,†], **Majid Pahlevani**[4], **Brett Bouma**[1,3], **Melissa J. Suter**[1], **Federico Capasso**[2,*], **Hamid Pahlevaninezhad**[1,2,*]

[1]Harvard Medical School and Massachusetts General Hospital, Boston, MA, USA.

[2]Harvard John A. Paulson School of Engineering and Applied Sciences, Harvard University, Cambridge, MA, USA.

[3]Harvard-MIT Health Science and Technology, Massachusetts Institute of Technology, Cambridge, MA, USA.

[4]Department of Electrical and Computer Engineering, Queen's University, Kingston, Ontario, Canada.

[5]Department of Mechanical and Materials Engineering, Queen's University, Kingston, Ontario, Canada.

Abstract

Microscopic imaging in three dimensions enables numerous biological and clinical applications. However, high-resolution optical imaging preserved in a relatively large depth range is hampered by the rapid spread of tightly confined light due to diffraction. Here, we show that a particular disposition of light illumination and collection paths liberates optical imaging from the restrictions imposed by diffraction. This arrangement, realized by metasurfaces, decouples lateral resolution from depth-of-focus by establishing a one-to-one correspondence (bijection) along a focal line between the incident and collected light. Implementing this approach in optical coherence tomography, we demonstrate tissue imaging at 1.3 μm wavelength with ~ 3.2 μm lateral resolution, maintained nearly intact over 1.25 mm depth-of-focus, with no additional acquisition or computation burden. This method, termed bijective illumination collection imaging, is general and might be adapted across various existing imaging modalities.

High-resolution imaging of tissue microstructures is instrumental to biology and enables numerous clinical applications. Optical microscopy using tightly focused light, however, cannot be maintained in a relatively large depth range due to rapid spread of light dictated

---

*Corresponding authors. capasso@seas.harvard.edu; hpahlevani@mgh.harvard.edu.
†Present address: Department of Photonics, National Yang Ming Chiao Tung University, Hsinchu, Taiwan.

by diffraction. Imaging modalities such as confocal[1] and two-photon[2] microscopies achieve high-resolution imaging only from a narrow region around a focal point. Thus, additional scanning mechanisms are necessary to axially translate the focal point with respect to the target for depth-resolved imaging[3]. This impedes rapid imaging and the imaging depth, often limited to a few hundred microns[4], is inadequate for many applications.

Using coherence gating, optical coherence tomography (OCT) captures real-time depth-resolved images of structures millimeters deep into the scattering tissue[5–9]. Though addressing axial resolution, OCT is still challenged by the competing lateral resolution and depth-of-focus due to diffraction that impedes high-resolution imaging in three-dimensions in a large depth range[10–12].

The central question is how light intensity should be distributed to obtain high-resolution imaging in three-dimensions within a large depth range. Focusing light on a single depth point, widely used in the existing imaging systems, yields arbitrary primacy to that point which is inconsistent with the goal of depth imaging. Alternatively, more equitable distribution of the optical intensity along the axial direction inevitably compromises lateral resolution due to diffraction.

Here, we present a concept termed bijective illumination collection imaging (BICI) to accomplish high-resolution imaging in three dimensions within a relatively large depth range. This is achieved through a particular disposition of illumination and collection paths that allows a one-to-one spatial correspondence (bijection) between the illumination and collection light defined exclusively along a focal line. The impact on imaging is demonstrated by applying BICI to overcome the limitations in high-resolution OCT. Metasurfaces[13–17] with the ability to impart tailored phases are used to realize the illumination and collection paths required for the implementation of BICI. We report ~ 3.2 μm lateral resolution maintained nearly intact over 1.25 mm imaging depth, ~12-fold larger imaging depth-of-focus compared to that obtained using an ideal Gaussian beam with the same lateral resolution. Imaging swine tracheobronchial tissue specimens indicates the BICI's prospect for high-resolution imaging preserved within a large depth range.

Concept

The boundaries of lateral resolution and depth-of-focus are coupled by diffraction (depth-of-focus ~ λ / NA^2 where λ is the wavelength and NA is the numerical aperture). There exists a class of so-called diffraction-free[18–23] solutions to the Helmholtz equation. However, these modes in their exact mathematical forms have spatially unbounded profiles (plane waves are a trivial example) and give rise to side lobes that carry a significant portion of the optical power (even in their physical realizations limited by a finite aperture). When used for imaging, the out-of-focus scattering from the side lobes compromises imaging resolution and sensitivity.

Revisiting lateral resolution and depth-of-focus in the context of imaging point spread function (PSF) provides opportunities to evade the restrictions imposed by diffraction. The PSF at any point is the product of the probabilities of photons illuminating (P_{ill}) and

collected from (P_{coll}) that point: PSF = $P_{ill} \times P_{coll}$[24,25] Based on this notion, it is possible to decouple lateral resolution from depth-of-focus using uniquely crafted illumination and collection paths.

In BICI, the illumination and collection paths are separated using two metasurfaces (arrays of nanoscale, subwavelength-spaced optical elements) positioned on two adjacent quadrants of a fictitious circle perpendicular to and centered at the imaging optical axis. Figure 1a,b depict schematics of an illumination beam impinging at right angle on one of the metasurfaces from a collimated source. Provided the illumination metasurface bends the ray incident on the point (r, θ) as defined in Fig. 1a by a constant angle β in the r-z plane, all the rays incident on the arc of radius r will cross a single point (focal point) on the z-axis (Fig. 1b). As a result, ray families originating from arcs of constant radii on the metasurface will form a continuous focal line along the z-axis (Fig. 1c). The collection metasurface (with a flip profile of the illumination metasurface with respect to the x-axis) forms ray sheets, mirror images of those in the illumination paths with respect to the x-z plane (Fig. 1d,e), that are the trajectories of the collected light. A snapshot of the illumination and collection beams in one of the lateral planes intersecting the focal line is illustrated in Fig. 1f.

Remarkably, this scheme yields invariant lateral resolution (determined by β) along the focal line whose length depends on the beam/metasurface size and β. In this configuration, illumination and collection paths overlap only on the focal points (Fig. 1f). This establishes a bijective relation defined exclusively on the focal line between the points illuminated and points from which light is collected, eliminating out-of-focus signals. This key bijective relation would be breached in case of any overlap between the illumination and collection beams other than those on the focal line. An example of such violation is illustrated for mispositioned illumination and collection beams in Supplementary Fig. 2.

In the existing high-resolution imaging systems, the effect of out-of-focus signals is typically lessened using tightly focused light to comparatively increase the signal from the focal point (using a confocal geometry or nonlinear effects at the focal point). This approach inevitably limits the depth range due to severe diffraction of tightly focused light. Indispensable to high-resolution imaging, BICI rejects out-of-focus signals using the uniquely crafted illumination and collection paths without compromising the depth range.

Design and comparison

To demonstrate the impact on imaging, we design BICI for a Fourier-domain OCT system in the near infrared range (~ 1300 nm ± 50 nm). The bending angle β and the beam/metasurface size are the main parameters governing lateral resolution and the length of the focal line. The design procedure and justifications are described in Supplementary Section 1. Wave analyses using a Fresnel-Kirchhoff integral[26] were performed to engineer the imaging PSF needed for the intended resolution and depth-of-focus. Design parameters are selected to achieve microscopic resolution imaging in a relatively large depth range (> 1mm) beyond which scattering becomes the dominant limitation. Given the design parameters (collimated beam size ~ 1.1 mm; β = 21°), wave analyses yield 3.2 μm full-width at half maximum

(FWHM) of PSF and 1.25 mm depth-of-focus defined as $1/e^2$ PSF intensity fall-off in the axial direction.

Figure 2 presents the results of an analytic comparison of BICI with the conventional approaches in terms of lateral resolution and depth-of-focus. An imaging system with a common path for illumination and collection using ideal Gaussian beams either matching BICI lateral resolution (3.2 μm, Fig. 2a) or its depth-of-focus (1.25mm, Fig. 2b) substantially compromises depth-of-focus (100 μm) or resolution (12 μm), respectively. A Bessel beam with the same FWHM of the central lobe (3.2 μm), though offers an extended depth-of-focus, suffers from side lobes that carry a significant portion of optical power[27,28] as illustrated in Fig. 2c. In contrast, BICI maintains a sharp PSF along a relatively large axial range (Fig. 2d) with negligible contributions from out-of-focus signals.

Implementation and validation

Figure 3a shows how BICI is incorporated through one arm of an interferometer. Target is axially positioned to overlap the focal line created by the metasurfaces. The distribution and geometry of pillars on metasurfaces are engineered to realize the illumination and collection beams in BICI. Based on the generalized Snell's law[13], the phase Φ required to bend ray sheets (as defined in Fig. 1b) with the angle β in the r-z plane satisfies

$$\frac{d\Phi(r)}{dr} = -\frac{2\pi}{\lambda_d}\sin(\beta) \tag{1}$$

where $\lambda_d = 1300$ nm is the design wavelength corresponding to the center wavelength of the OCT source. This phase was realized by metasurfaces comprised of square amorphous silicon (a-Si) nanopillars with the same height (750 nm) distributed on a square lattice (370 nm unit cell). Nanopillars of varying base sizes across the lattice impart the required local phase. Calculations of the nanopillars' cumulative phase and transmittance are detailed in Supplementary Section 2. Owing to its high refractive index and low absorption in the near infrared range[29–31], a-Si is a suitable material to achieve efficient metasurfaces (> 70% of the incident power concentrated on the focal line) for this application. Metasurfaces (Fig. 3b,c) were fabricated on a glass substrate using electron beam lithography[30,32]. The linear phase profile in Eq. (1) can also be realized using an axicon. However, as detailed in Supplementary Section 1, the implementation using metasurfaces gives rise to several advantages including superior depth-of-focus for a given resolution, ease of implementation, and feasibility of miniaturization for endoscopic applications.

The intensity profiles of the illumination and collection beams were measured using a custom-built optical setup (Supplementary Fig. 13). The measured illumination (Fig. 4a) and collection (Fig. 4b) beams form coincident focal lines along the z-axis. Figure 4c indicates a sharp imaging PSF (the product of the illumination and collection intensity profiles) with small FWHMs (~ 3.7 μm at z = 0) maintained over a relatively large depth range (~ 1.22 mm). These measurements are consistent with the results of wave analysis (3.2 μm FWHM; 1.25 mm depth-of-focus), though slight deviations exist likely due to the non-linear response of the camera, alignment imperfections of the optical setup, and/or fabrication errors. Despite the chromatic dispersion of the metasurfaces[33–37], the focal lines

of the illumination and collection beams remain aligned over the entire spectrum of the light source with no significant changes in the imaging PSF as illustrated in Supplementary Section 1.

BICI was characterized in terms of lateral resolution and depth-of-focus through imaging a resolution target made of a subwavelength gold line (200 nm width and 50 nm height) fabricated on a glass substrate. BICI was coupled to an in-house Fourier-domain OCT system[38,39] (Supplementary Section 4). As illustrated in Fig. 5a, lateral resolution and depth-of-focus were measured by scanning the gold line across the focal line at varying target-metasurface distances. Figure 5b shows the imaging PSF measured at three selected depth points (Supplementary Fig. 16 contains the complete sets of measurements). Summarized in Fig. 5c, results indicate high lateral resolution (~ 3.28 μm) maintained over more than 1.25 mm depth range, consistent with our anticipations from the wave analysis. To demonstrate the improvements, Fig. 5c also includes the analytical imaging PSF with an ideal Gaussian beam of the same lateral resolution that proves reduced imaging depth-of-focus (~ 12 times) compared to that of BICI.

There are also techniques in which mathematically optimized phase profiles are imparted using freeform metasurfaces to obtain maximum depth-of-focus[40–43]. Although these techniques can somewhat alleviate the issue through a modest increase in depth-of-focus (~ 1.5 – 2 times), they cannot be considered as a strategy to radically overhaul the limitations in the maintenance of high-resolution imaging across a relatively large depth range.

Imaging

We assessed the BICI capabilities to visualize tissue structures in the pulmonary airways of swine ex vivo. Freshly excised tracheobronchial tissue specimens were prepared and imaged by BICI and, consecutively, by a conventional approach with common illumination collection paths using a standard plano-convex lens (LA1951-C, Thorlabs, NJ). Detailed in Supplementary Section 4, this lens was chosen to match the imaging depth-of-focus achieved by BICI (~ 1.5 mm). Tissue specimens were laterally scanned using an automated motorized translation stage.

Figure 6 shows the images captured by BICI (Fig. 6b,d,f,h) and the conventional approach (Fig. 6a,c,e,g). Comparison indicates that BICI visualizes bronchial tissue microstructures with superior resolving power preserved in a relatively large depth range. Figure 6b highlights the BICI ability to distinctly visualize inflammatory infiltrate, poorly visible in the image captured by the conventional approach (Fig. 6a). Clear delineation of tissue layers including epithelium, lamina propria, and cartilage deep into the tissue are illustrated in Fig. 6d,f. This indicates that BICI provides markedly higher resolution and yet maintains a large imaging depth range nearly matching that of the conventional approach (Fig. 6c,e). Glandular patterns are also visualized by BICI in Fig. 6f which are not clearly discernable in Fig. 6e captured by the conventional approach.

Figure 6g,h shows the results in a case where the trachea tissue specimen underwent histological processes following optical imaging. Compared to the image of the conventional

approach (Fig. 6g), the image captured using BICI (Fig. 6h) carries more detailed morphological information closer to that provided in the histology image (Fig. 6i). As an illustration, while poorly visible in Fig. 6g, perichondrium wrapping around cartilage is distinctly contrasted in Fig. 6h captured by BICI.

Comparison of images captured by BICI with those of the conventional approach indicates reduced speckles of the former. Detailed in Discussion, this is due mainly to the BICI's higher lateral resolution maintained along the depth range as well as its ability to eliminate out-of-focus and back-reflection signals.

The images shown in Fig. 6 were captured at the same illumination power (~ 18 mW) in BICI and in the conventional approach. The beam arrangement in BICI results in a narrower angular range of the light collected from the points on the focal line in BICI compared to that collected by an ideal diffraction-limited lens at its focal point. This implies that the signal level at the points along the focal line in BICI is smaller than that at the focal point when imaging with an ideal diffraction-limited lens. However, this is not the case for other points along the depth range (except for the focal point) in the latter which renders it inpat for depth imaging. Evident from images presented in Fig. 6, this does not pose any issue in this work where BICI is applied to OCT, a highly sensitive imaging modality with significant dynamic range. In addition, the BICI ability to eliminate out-of-focus signals and back-reflection from imaging optics significantly reduces the noise level.

Discussion

The presented images in this work are a testament to the impact of BICI on imaging quality. BICI entails no additional processing[44] or acquisition[10] burden and can be implemented across various wavelength ranges as its working principles remain unaltered with a wavelength change. For instance, BICI can be implemented in broadband OCT systems operating at shorter wavelengths with improved axial resolution. The wavelength range in this work is chosen to avoid increased scattering at shorter wavelengths that predominantly limits the imaging depth[10,45,46].

Various configurations of illumination and collection beams were previously reported in OCT (for speckle-reduction[47,48] and deep tissue imaging[49]), in two-photon microscopy (for enhanced signal-to-background ratio[50–52]),in theta confocal[25,53], 4pi[54], and light sheet[55] microscopy (for improved resolution), and dark-field microscopy[56] (for enhanced sensitivity). These systems are designed to capture signals from a region neighboring a single focal point. Aa a result, imaging within a modest depth range entails either using very small NA[47–49] (compromising lateral resolution) or physical translation of the target with respect to the imaging system[25,50–56] (compromising imaging speed).

Sensibly, the optical arrangement for depth imaging with preserved lateral resolution should 1) focus light equitably along the depth range (on a focal line), and 2) reject out-of-focus signals originating from the points outside the focal line. Unlike the previous works, the optical arrangement devised in BICI meets both criteria, enabling imaging relatively large depth range along which the lateral resolution is maintained.

OCT, being a coherence imaging technique, comprises of speckles which are carriers of information and, at the same time, a source of noise[57]. The signal-degrading speckles are due mainly to the effects of multiple backscatters, while the signal-carrying speckles are the result of the single back-scattered component whose spatial frequency content extends to the diffraction limit of the imaging optics[57]. Scaling up proportionally to the spot size, the signal-carrying speckles originate from the focal zone and the signal-degrading speckle is created by out-of-focus light scattered multiple times. Evident from images in Fig. 6, compared to the conventional approach, BICI suffer considerably less from the effects of speckles due to: 1) its higher lateral resolution maintained along the depth range, resulting in notably smaller speckle sizes, 2) the ability to eliminate out-of-focus signal and, in turn, the effects of multiple scattering, and 3) the ability to reject back-reflection from imaging optics.

Pathological changes at early stages of diseases like cancers are often very subtle and can be easily overlooked. In vivo high-resolution imaging maintained in a large depth range has the potential to enable early and accurate detection and diagnosis. Being implemented using metasurfaces, BICI can be feasibly miniaturized into endoscopic devices[58,59] for in vivo high-resolution imaging of internal organs.

The advent of high-resolution optical imaging techniques has impacted fundamental medical research as well as clinical applications. Expanding the scope of applications, however, necessitates overcoming major limitations in the current techniques. The diffraction-imposed trade-off between lateral resolution and depth-of-focus is circumvented through bijective illumination collection imaging, enabling high-resolution imaging in three dimensions. Though BICI is applied to OCT in this work, the underlying concept is general and might be adapted across various imaging modalities such as confocal and two-photon microscopy.

Methods

Fabrication process.

The metasurfaces were fabricated using a top-down lithography technique[30,32]. A 750 nm thick a-Si layer was deposited on a glass substrate using the plasma-enhanced chemical vapor deposition. Electron beam lithography (EBL) was used to create the intended pattern on the negative tone photoresist (Micro resist technology, ma-N 2403). Deep reactive ion etching was then used to generate a-Si nanopillars.

The resolution target was also fabricated by EBL of a line pattern on the positive tone photoresist (Zeon Chemicals, ZEP520A), followed by deposition of a gold layer with 50 nm thickness using thermal evaporation and lift-off.

Supplementary Material

Refer to Web version on PubMed Central for supplementary material.

Acknowledgements.

Data and materials availability.

All data generated and analysed are included in the paper and its supplementary information. The imaging data presented in Fig. 6 are available at https://figshare.com/articles/figure/ Fig_6e_TIF/17124062.

References

1. Stephens DJ & Allan VJ Light microscopy techniques for live cell imaging. Science. 300, 82–86 (2003). [PubMed: 12677057]

2. Denk W, Strickler JH & Webb WW Two-photon laser scanning fluorescence microscopy. Science. 248, 73–76 (1990). [PubMed: 2321027]

3. Beaulieu DR, Davison IG, Kılıç K, Bifano TG & Mertz J Simultaneous multiplane imaging with reverberation two-photon microscopy. Nat. Methods 17, 283–286 (2020). [PubMed: 32042186]

4. Helmchen F & Denk W Deep tissue two-photon microscopy. Nat. Methods 2, 932–940 (2005). [PubMed: 16299478]

5. Huang D et al. Optical coherence tomography. Science. 254, 1178–1181 (1991). [PubMed: 1957169]

6. Fujimoto JG et al. Optical biopsy and imaging using optical coherence tomography. Nat. Med 1, 970–972 (1995). [PubMed: 7585229]

7. Tearney GJ et al. In vivo endoscopic optical biopsy with optical coherence tomography. Science. 276, 2037–2039 (1997). [PubMed: 9197265]

8. Fujimoto JG Optical coherence tomography for ultrahigh resolution in vivo imaging. Nat. Biotechnol 21, 1361–1367 (2003). [PubMed: 14595364]

9. Vakoc BJ, Fukumura D, Jain RK & Bouma BE Cancer imaging by optical coherence tomography: Preclinical progress and clinical potential. Nat. Rev. Cancer 12, 63–368 (2012).

10. Zhou KC, Qian R, Degan S, Farsiu S & Izatt JA Optical coherence refraction tomography. Nat. Photonics 13, 794–802 (2019). [PubMed: 35386729]

11. Curatolo A et al. Quantifying the influence of Bessel beams on image quality in optical coherence tomography. Sci. Rep 6, 23483 (2016). [PubMed: 27009371]

12. Zhang M, Ren Z & Yu P Improve depth of field of optical coherence tomography using finite energy Airy beam. Opt. Lett 44, 3158–3161 (2019). [PubMed: 31199405]

13. Yu N et al. Light propagation with phase discontinuities: Generalized laws of reflection and refraction. Science. 334, 333–337 (2011). [PubMed: 21885733]

14. Lin D, Fan P, Hasman E & Brongersma ML Dielectric gradient metasurface optical elements. Science. 345, 298–302 (2014). [PubMed: 25035488]

15. Yu N & Capasso F Flat optics with designer metasurfaces. Nat. Mater 13, 139–150 (2014). [PubMed: 24452357]

16. Khorasaninejad M et al. Metalenses at visible wavelengths: Diffraction-limited focusing and subwavelength resolution imaging. Science. 352, 1190–1194 (2016). [PubMed: 27257251]

17. Khorasaninejad M & Capasso F Metalenses: Versatile multifunctional photonic components. Science. 358, eaam8100 (2017). [PubMed: 28982796]

18. Durnin J, Miceli JJ & Eberly JH Diffraction-free beams. Phys. Rev. Lett 58, 1499–1501 (1987). [PubMed: 10034453]

19. Berry MV & Balazs NL Nonspreading wave packets. Am. J. Phys 47, 264–267 (1979).

20. Gutierrez-Vega JC, Iturbe-Castillo MD & Chavez-Cerda S Alternative formulation for invariant optical fields: Mathieu beams. Opt. Lett 25, 1493–1495 (2000). [PubMed: 18066256]

21. Bandres MA, Gutierrez-Vega JC & Chavez-Cerda S Parabolic nondiffracting optical wave fields. Opt. Lett 29, 44–46 (2004). [PubMed: 14719655]

22. Lopez-Mariscal C, Bandres MA, Gutierrez-Vega JC & Chavez-Cerda S Observation of parabolic nondiffracting optical fields. Opt. Express 13, 2364–2369 (2005). [PubMed: 19495126]

23. Fahrbach FO, Simon P & Rohrbach A Microscopy with self-reconstructing beams. Nat. Photonics 4, 780–785 (2010).

24. Webb RH Confocal optical microscopy. Rep. Prog. Phys 59, 427–471 (1996).

25. Stelzer EHK & Steffen L Fundamental reduction of the observation volume in far-field light microscopy by detection orthogonal to the illumination axis: confocal theta microscopy. Opt. Commun 111, 536–547 (1994).

26. Born M & Wolf E Principles of Optics. (Pergamon Press, 1970).

27. Blatter C et al. Extended focus high-speed swept source OCT with self-reconstructive illumination. Opt. Express 19, 12141–12155 (2011). [PubMed: 21716451]

28. Lorenser D, Christian Singe C, Curatolo A & Sampson DD Energy-efficient low-Fresnel-number Bessel beams and their application in optical coherence tomography. Opt. Lett 39, 548–551 (2014). [PubMed: 24487862]

29. Fattal D, Li J, Peng Z, Fiorentino M & Beausoleil RG Flat dielectric grating reflectors with focusing abilities. Nat. Photonics 4, 466–470 (2010).

30. Khorasaninejad M & Crozier KB Silicon nanofin grating as a miniature chirality-distinguishing beam-splitter. Nat. Commun 5, 5386 (2014). [PubMed: 25388102]

31. Arbabi A, Horie Y, Ball AJ, Bagheri M & Faraon A Subwavelength-thick lenses with high numerical apertures and large efficiency based on high-contrast transmitarrays. Nat. Commun 6, 7069 (2015). [PubMed: 25947118]

32. Khorasaninejad M & Capasso F Broadband multifunctional efficient meta-gratings based on dielectric waveguide phase shifters. Nano Lett. 15, 6709–6715 (2015). [PubMed: 26372331]

33. Khorasaninejad M et al. Achromatic metasurface lens at telecommunication wavelengths. Nano Lett. 15, 5358–5362 (2015). [PubMed: 26168329]

34. Khorasaninejad M, Chen WT, Oh J & Capasso F Super-dispersive off-axis metalenses for compact high resolution spectroscopy. Nano Lett. 16, 3732–3737 (2016). [PubMed: 27119987]

35. Khorasaninejad M et al. Achromatic metalens over 60 nm bandwidth in the visible and metalens with reverse chromatic dispersion. Nano Lett. 17, 1819–1824 (2017). [PubMed: 28125234]

36. Arbabi E, Arbabi A, Kamali SM, Horie Y & Faraon A Controlling the sign of chromatic dispersion in diffractive optics with dielectric metasurfaces. Optica 4, 625–632 (2017).

37. Chen WT et al. A broadband achromatic metalens for focusing and imaging in the visible. Nat. Nanotechnol 13, 220–226 (2018). [PubMed: 29292382]

38. Yun SH, Tearney GJ, de Boer JF & Bouma BE Removing the depth-degeneracy in optical frequency domain imaging with frequency shifting. Opt. Express 12, 4822–4828 (2004). [PubMed: 19484034]

39. Yun SH et al. Comprehensive volumetric optical microscopy in vivo. Nat. Med 12, 1429–1433 (2006). [PubMed: 17115049]

40. Huang L, Whitehead J, Colburn S & Majumdar A Design and analysis of extended depth of focus metalenses for achromatic computational imaging. Photonics Res. 8, 1613–1623 (2020).

41. Bayati E et al. Inverse Designed Metalenses with Extended Depth of Focus. ACS Photonics 7, 873–878 (2020).

42. Colburn S & Majumdar A Simultaneous Achromatic and Varifocal Imaging with Quartic Metasurfaces in the Visible. ACS Photonics 7, 120–127 (2020).

43. Colburn S, Zhan A & Majumdar A Metasurface optics for full-color computational imaging. Sci. Adv 4, 2114 (2018).

44. Ralston TS, Marks DL, Carney PS & Boppart SA Interferometric synthetic aperture microscopy. Nat. Phys 3, 129–134 (2007). [PubMed: 25635181]

45. Liu L et al. Imaging the subcellular structure of human coronary atherosclerosis using micro-optical coherence tomography. Nat. Med 17, 1010–1014 (2011). [PubMed: 21743452]

46. Yuan W, Brown R, Mitzner W, Yarmus L & Li X Super-achromatic monolithic microprobe for ultrahigh-resolution endoscopic optical coherence tomography at 800 nm. Nat. Commun 8, 1531 (2017). [PubMed: 29142274]

47. Desjardins AE et al. Angle-resolved Optical Coherence Tomography with sequential angular selectivity for speckle reduction. Opt. Express 15, 6200–6209 (2007). [PubMed: 19546925]

48. Klein T, Raphael A, Wolfgang W, Tom P & Huber R Joint aperture detection for speckle reduction and increased collection efficiency in ophthalmic MHz OCT. Biomed. Opt. Express 4, 619–634 (2013). [PubMed: 23577296]

49. Zhao Y et al. Dual-axis optical coherence tomography for deep tissue imaging. Opt. Lett 42, 2302–2305 (2017). [PubMed: 28614337]

50. Cheng X et al. Comparing the fundamental imaging depth limit of two-photon, three-photon, and non-degenerate two-photon microscopy. Opt. Lett 45, 2934–2937 (2020). [PubMed: 32412504]

51. Wang C, Qiao L, Mao Z, Cheng Y & Xu Z Reduced deep-tissue image degradation in three-dimensional multiphoton microscopy with concentric two-color two-photon fluorescence excitation. J. Opt. Soc. Am. B 25, 976–982 (2008).

52. Kobat D, Zhu G & Xu C Background reduction with two-color two-beam multiphoton excitation. Biomed. Opt. OSA Tech. Dig. (Optical Soc. Am. 2008) BMF6 (2008) doi:10.1364/biomed.2008.bmf6.

53. Liu JTC et al. Dual-axes confocal reflectance microscope for distinguishing colonic neoplasia. J. Biomed. Opt 11, 054019 (2006). [PubMed: 17092168]

54. Hell S & Stelzer EHK Properties of a 4Pi confocal fluorescence microscope. J. Opt. Soc. Am. A 9, 2159–2166 (1992).

55. Power RM & Huisken J A guide to light-sheet fluorescence microscopy for multiscale imaging. Nat. Methods 14, 360–373 (2017). [PubMed: 28362435]

56. Gao PF, Lei G & Huang CZ Dark-Field Microscopy: Recent Advances in Accurate Analysis and Emerging Applications. Anal. Chem 93, 4707–4726 (2021). [PubMed: 33620210]

57. Schmitt JM, Xiang SH & Yung KM Speckle in optical coherence tomography. J. Biomed. Opt 4, 95–105 (1999). [PubMed: 23015175]

58. Pahlevaninezhad H et al. Nano-optic endoscope for high-resolution optical coherence tomography in vivo. Nat. Photonics 12, 540–547 (2018). [PubMed: 30713581]

59. Gissibl T, Thiele S, Herkommer A & Giessen H Two-photon direct laser writing of ultracompact multi-lens objectives. Nat. Photonics 10, 554–560 (2016).
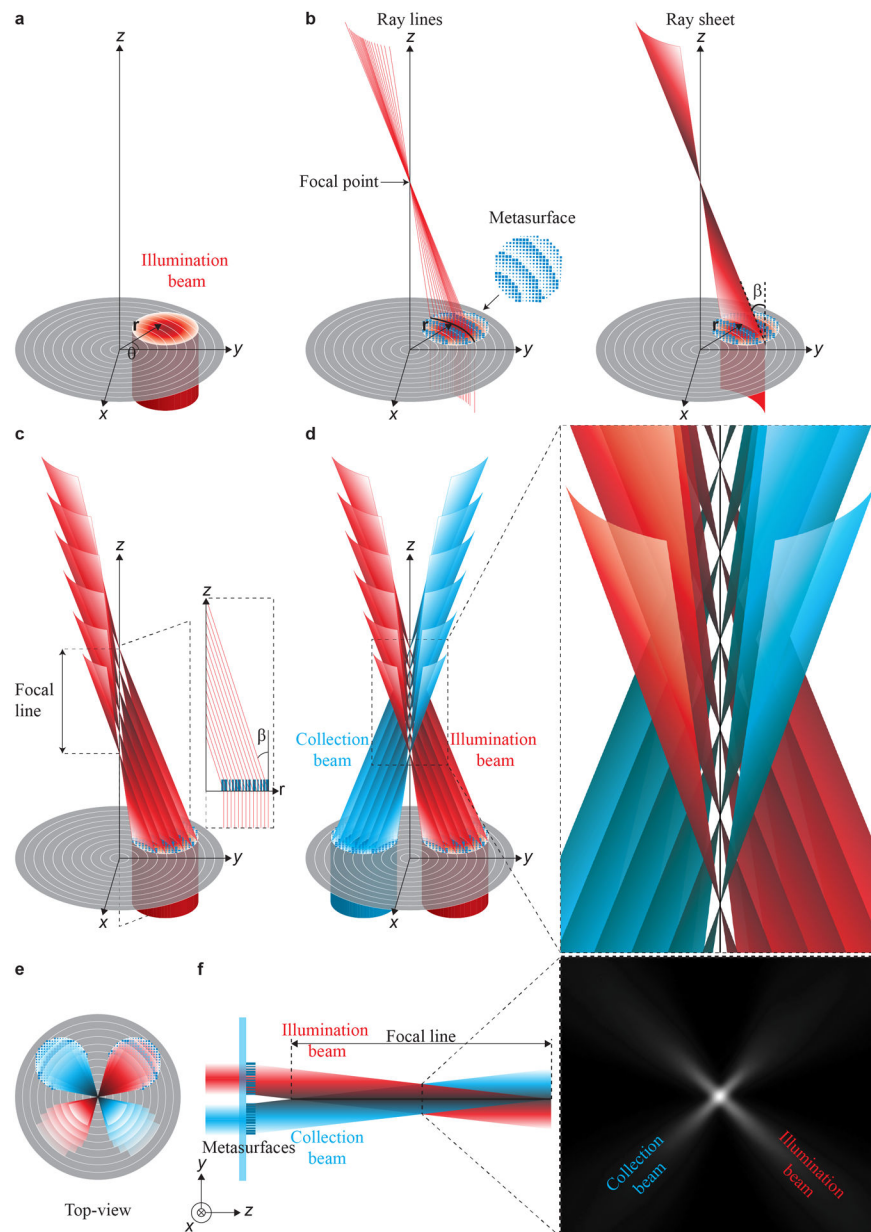
Author Manuscript

Author Manuscript

Author Manuscript

Author Manuscript

Fig. 1 |. BICI concept.

(**a**) The illumination beam is generated by collimated light positioned off the imaging optical axis. (**b**) The metasurface bends a ray family (sheet) originating from an arc of radius r by a constant angle β to form a focal point on the z-axis. A family of rays originating from the same arc is shown as a ray sheet. (**c**) Ray sheets subject to the same bending paradigm constitute a focal line along the z-axis. The focal line is continuous even though a finite number of focal points is illustrated for clarity. (**d**) The collection metasurface establishes trajectories of collected light in ray sheets, mirror images of illumination paths with respect to the x-z plane. This configuration enables a one-to-one correspondence, i.e. a bijective relation between the focal points of the illumination and collection paths, to eliminate out-of-focus signals. Magnified inset manifests the bijective relation. (**e**) Top-view

of the illumination and collection beams. (**f**) Schematic of the illumination and collection beams and a snapshot captured by a camera from one of the lateral planes intersecting the focal line, illustrating the actual arrangement of illumination and collection paths. This arrangement allows only the collection of photons originating from the corresponding illumination focal point.
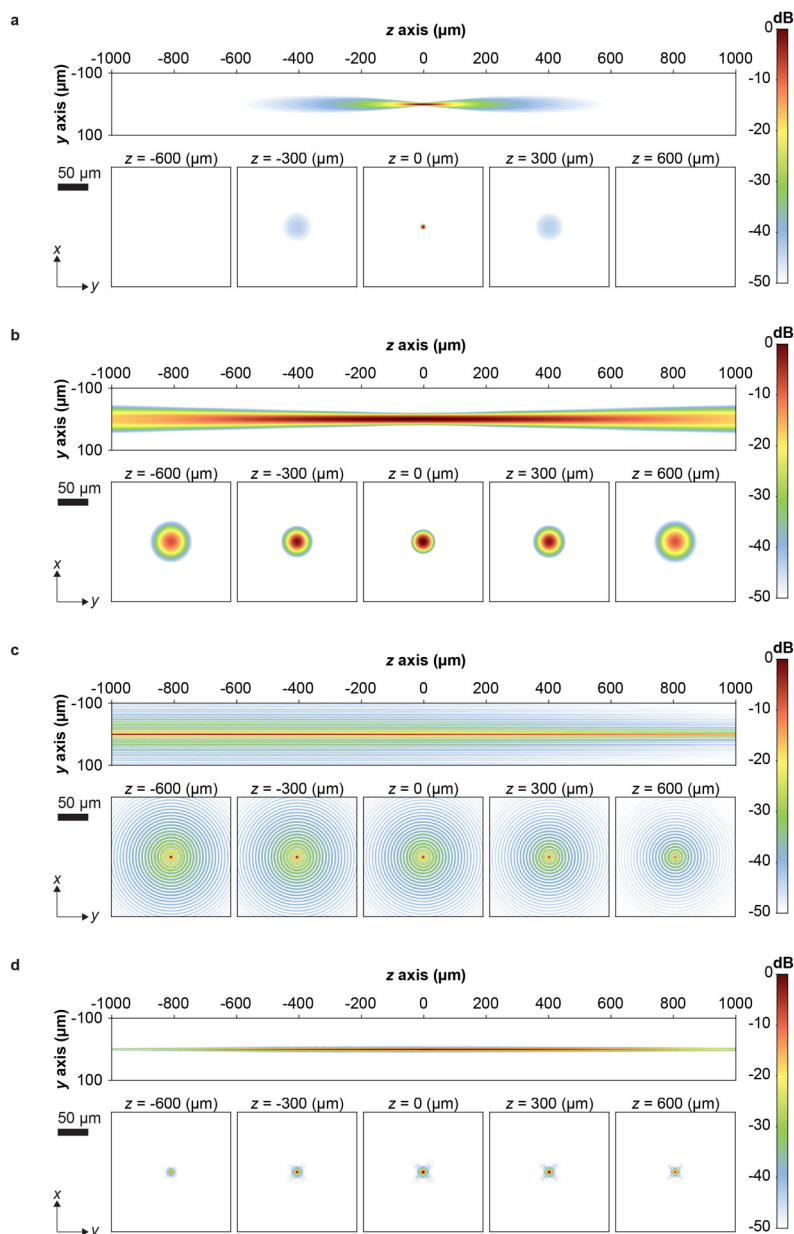
Fig. 2 |. Analytic PSF comparison of BICI with those using common path Gaussian and Bessel beams.

(**a**) The PSF of a tightly focused Gaussian beam (~ 3.2 μm FWHM) rapidly degrades away from the focal point. (**b**) The PSF of a Gaussian beam with a relatively large depth-of-focus (~ 1.25 mm) assumes greatly compromised lateral resolution. (**c**) The PSF of a Bessel beam with 3.2 μm FWHM of central lobe involves spread of power into several side lobes detrimental to imaging quality. (**d**) The PSF of BICI designed for ~ 3.2 μm lateral resolution and ~ 1.25 mm depth-of-focus. Unlike the Gaussian and Bessel beams, BICI maintains a sharp PSF over a large depth range.
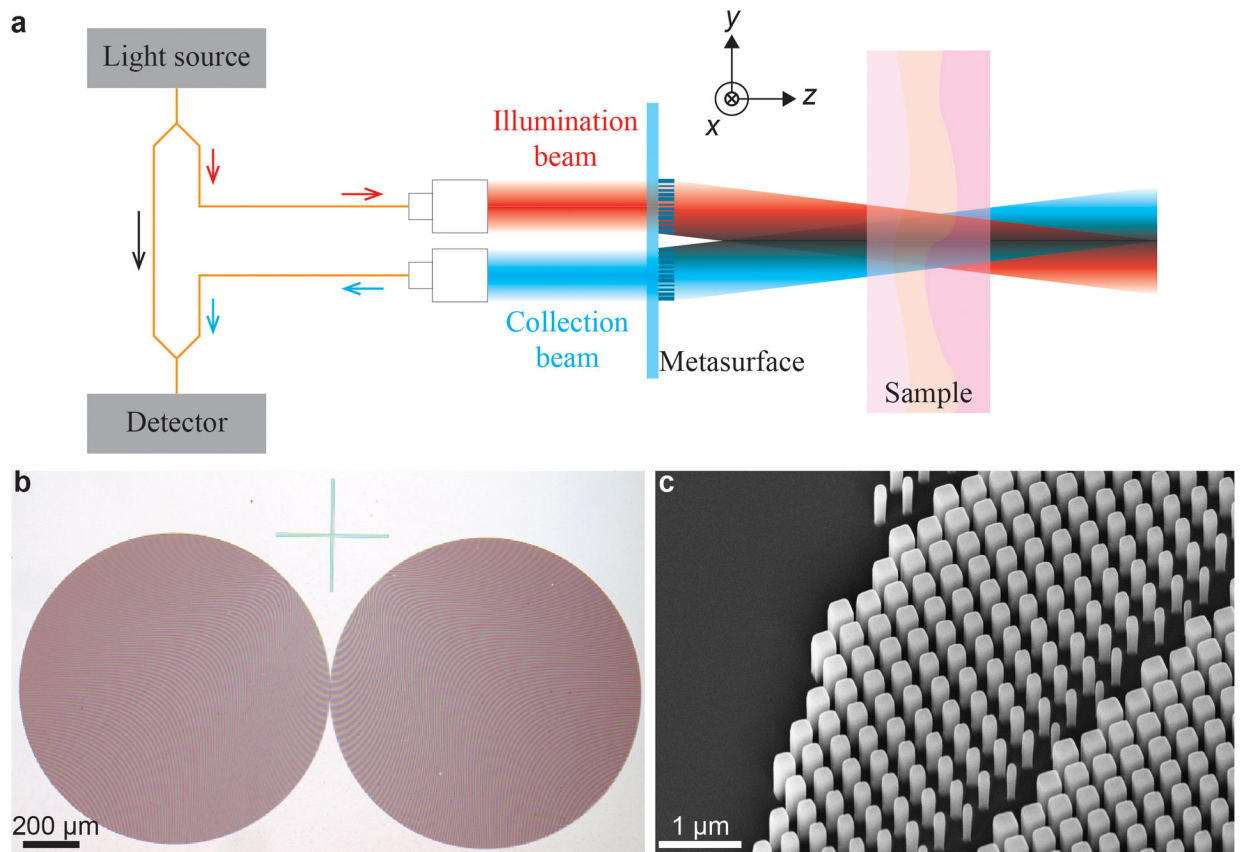
Fig. 3 |. BICI implementation.
(**a**) Incorporation of BICI through one arm of an interferometer (orange lines represent single mode fiber). (**b**) Widefield optical image of the fabricated illumination and collection metasurfaces each 1.1mm in diameter. The mark between the two metasurfaces coincides with the imaging optical axis. (**c**) A scanning electron micrograph of the fabricated metasurface consisting of square a-Si nanopillars.
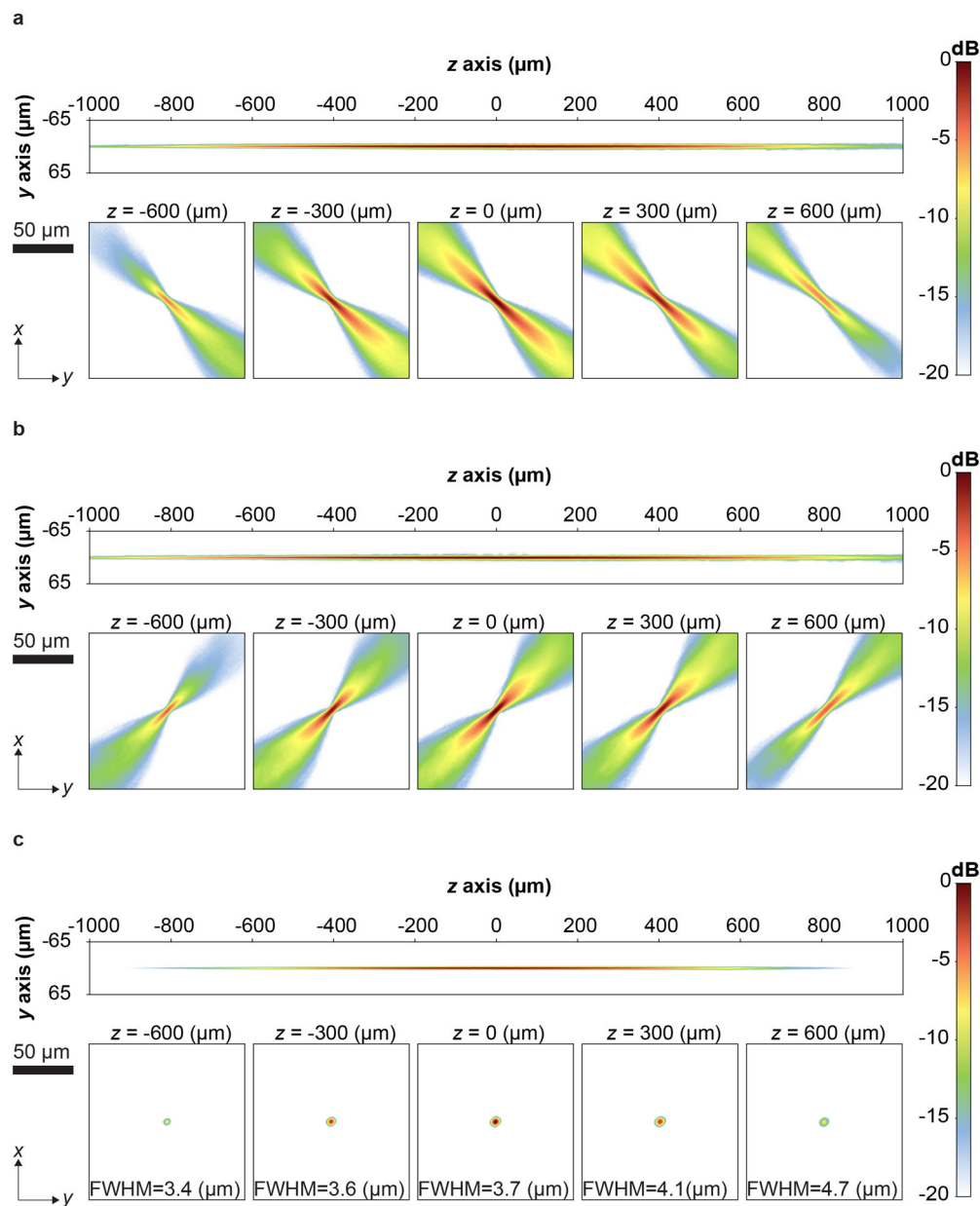
Fig. 4 |. Characterization of the BICI PSF.

Intensity distribution measurements of the illumination (**a**) and collection (**b**) beams in the x-z and x-y planes at 1300 nm wavelength. The illumination and collection beams overlap only on the focal line along the z-axis, demonstrating the bijective architecture. (**c**) The imaging PSF, the product of the illumination and collection intensity profiles, indicates the maintenance of a sharp PSF in a large axial range. The position z = 0 is ~ 2 mm away from the metasurfaces.
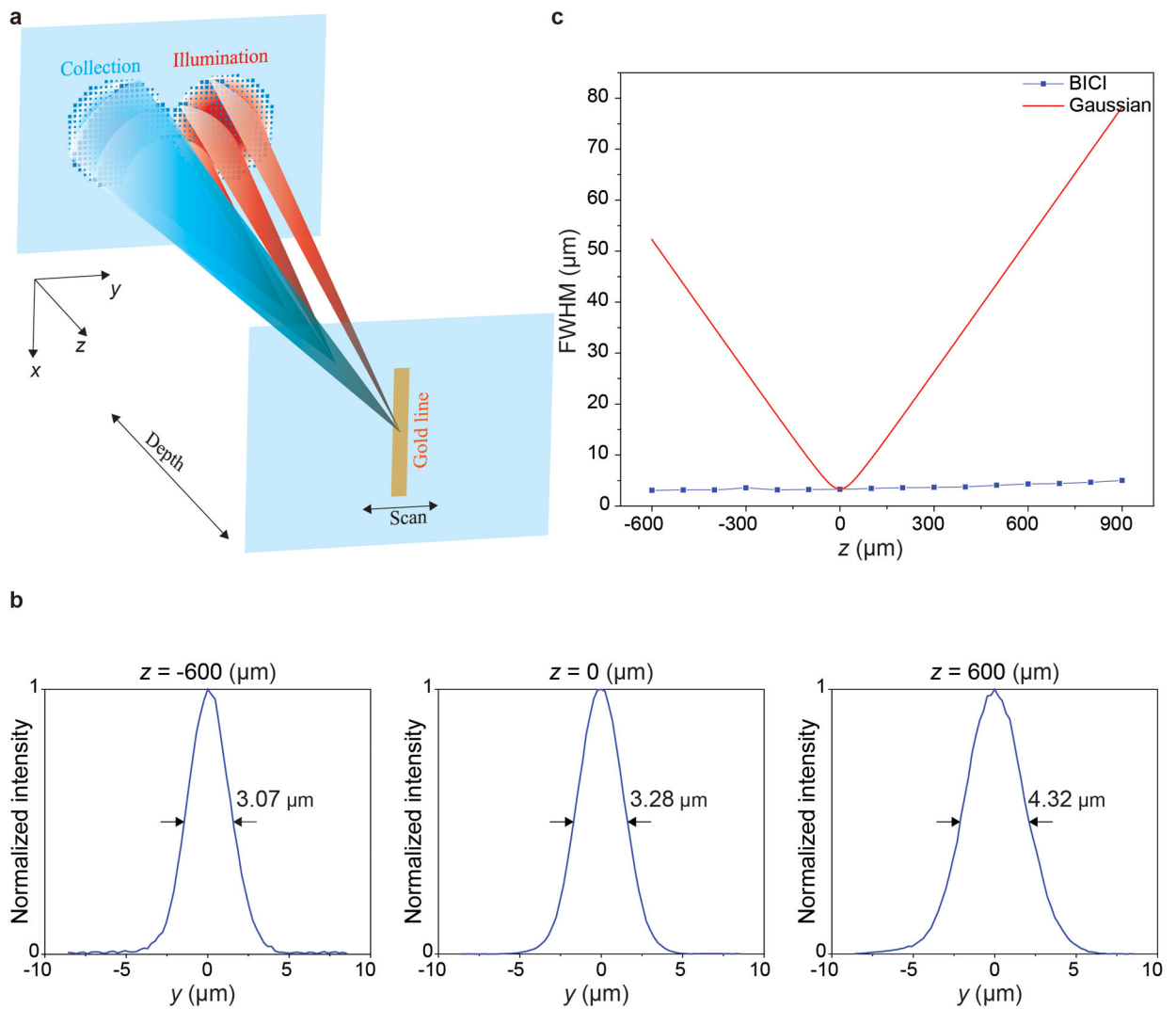
Fig. 5 |. BICI resolution and depth-of-focus measurement.
(**a**) Schematic of the measurement setup for imaging a subwavelength gold line being scanned across the focal line at various depth points. (**b**) Measured imaging PSF at three depth points. (**c**) The measured resolution of BICI is compared to the theoretical resolution obtained from a Gaussian beam (in a common path illumination-collection scheme) of the same lateral resolution, highlighting the BICI ability to maintain high resolution in a large depth range. The position z = 0 located ~ 2 mm away from the metasurfaces.
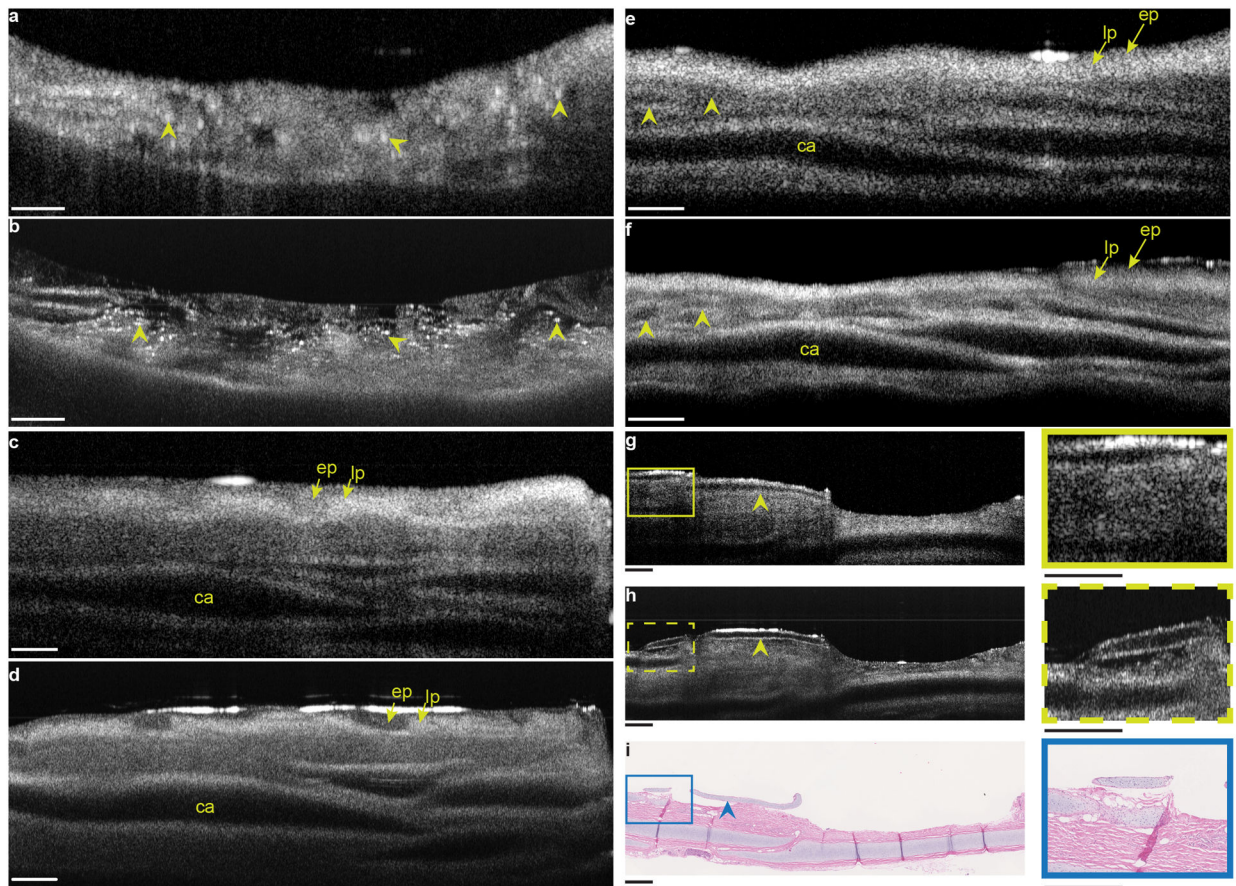
Fig. 6 |. Tissue imaging comparison of BICI and a conventional approach.
Imaging swine tracheobronchial tissue specimens using a plano-convex lens with common illumination and collection paths (**a**, **c**, **e**, **g**) and BICI (**b**, **d**, **f**, **h**). BICI provides a distinct view of the trachea tissue microstructures in (b) including inflammatory infiltrate (arrowheads), poorly visible in (a) captured by the conventional approach. Airway tissue layers including epithelium (ep), lamina propria (lp), and cartilage (ca) are clearly delineated in (d and f). Arrowheads in (e) and (f) indicate glandular patterns visualized by BICI which are not clearly discernable in the image of the conventional approach. (**i**) Corresponding histology image of the tissue imaged by the conventional approach (g) and BICI (h). BICI provides more detailed morphological information, closer to the structures identified in the histology image. Arrowheads indicate clearly contrasted perichondrium wrapping around cartilage in the BICI image (h) which is poorly visible in (g). Scale bars, 500 μm.